Egypt. J. Chem. **Vol. 65,** No. SI13B pp. 1333 - 1345 (2022)

Egyptian Journal of Chemistry

http://ejchem.journals.ekb.eg/

RAMAN MICRO-SPECTROSCOPIC INVESTIGATION OF CORROSION PRODUCTS.

Diaa Atta, [*a,b] **, Saleh Ahmed**[c]**, Mohamed Abdelbar**[d]

[a] *Spectroscopy department, Physics Research Institute, National Research Centre, 33 El Behooth St., Dokki, Giza, Egypt, Affiliation ID: 60014618*

[b] *Nonlinear optics and fluorescence Unit, Physics Research Institute, National Research Centre-Dokki, Cairo 12622, Egypt, Affiliation ID: 60014618.*

[c] *Conservation Department, Faculty of Archaeology, Fayoum University, Al-Fayoum Governorate, Egypt*

[d] *Conservation Department, Faculty of Archaeology, Damietta University, Damietta El-Gadeeda City, Damietta Governorate, 34511, Egypt.*

Abstract

Selected four gilt-bronze statuettes have been studied after excavation from the burial environment. Soil deposits and corrosion forms were observed on the surface disfiguring the gold layer. Confocal micro-Raman spectroscopy and Portable X-ray fluorescence (pXRF) were used to identify the molecular structure and elements distribution over the statuette's surfaces. Total internal reflection fluorescence (TIRF) has been utilized to recognize the surface/interface state before the conservation treatment and takes the high-resolution imaging. Chemical analyses indicated that it was made of leaded bronze. A high lead content in the statuettes was reflected by lead corrosion products admixed with green chloride and carbonate salts of copper. Conservation treatment was accomplished using fine and appropriate mechanical tools to recover all the gilding remains and surface details. Finally, the protection process of statuettes was accomplished using two layers of Permalac.

Keywords: *Corrosion; Gilt-bronze patina; Raman Spectroscopy; Confocal Microscope; X-ray fluorescence; Conservation Treatment*

.

1. Introduction

In the last decade, micro-Raman spectroscopy was used in the characterization of the bronze corrosion artifacts under burial conditions was one of the most investigated subjects. Characterization tools for cultural heritage are of importance for characterizing the archaeological items. Vibrational spectroscopy like FTIR and Raman spectroscopy plays an important role in identifying the item structure on the molecular level [1-6]. Combining molecular modeling with the experimental techniques plays a very important role in both assigning the spectral charts and treating the surfaces of the monument with new compounds as protective layers [7-11]. Enhancing the traditional techniques by combination with imaging techniques like confocal microscopy enhances the monitoring of the studied samples. The ultra-super resolution techniques which depend on fluorescence, like single-molecule and time-resolved systems [12-17].

Micro-Raman spectroscopy is well set as one of the most important molecular spectroscopic techniques based on laser radiation. Optimizing the laser power and confocal volume in micro-Raman spectroscopy helps so much in collecting valuable data from the resulting Raman spectra and maps [18-19]. It is a non-destructive technique; very small specimen meets the purpose, appropriate in situ evaluation, and making 3D images. This technique can be applied for analyses the composite objects as gilt bronze statuette. Concerning the study of corrosion phases, the methodological approach has advanced over time. Raman spectroscopy developed the characterization of the chemical structure of the archaeological materials. In the case of conservation science, XRF could be regarded as a powerful technique, it could measure the atomic concentration with high precision for a wide range of materials, especially the metallic archaeological objects [20-22]. Archaeological artefacts that may remain in the soil for the long-term are subjected to severe corrosion. Corrosion ratio in the burial condition depends on soil structure, salinity, pH, dissolved oxygen, temperature, and relative

---

*Corresponding author e-mail: diaalolo2004@gmail.com

Receive Date: 1 August 2022, Revise Date: 15 August 2022, Accept Date: 30 August 2022

DOI: 10.21608/EJCHEM.2022.155709.6728

humidity, moreover microbiological activity. When a gilded bronze is buried in soil that is saturated with pollutants and salts, the object's surface interacts with the surrounding compounds, producing a green and blue bronze patina. In the burial environment, the salt solutions are rich with ions hence the conductivity is also high, while we have gold and copper so expected electrodes are present in such ion reach solution [23]. In this case, an active electric cell arises between the two metals differs in electrochemical potential in the presence of electrolytic solution.

Gold acted as a cathodic terminal and copper is progressively corroded [24]. The cuprite layer is the usual component found below the gilding layer, and either carbonate or tri-hydroxy chloride compounds are found on the gilding layer, that turns it to a very fragile and porous [25-26].

The objective of this work is to identify the chemical structure of the gilt-bronze statuettes and measure the degradation mechanism in the burial environment by micro-Raman and Portable and X-ray Fluorescence. Optimum parameters of the Raman micro-spectroscopy like laser power density and laser exposure time were used to set this study on gilt bronze samples without affecting the chemical structure of the alloy and the corrosion products.

2. Experimental and Methods

Artefacts Description:

The statuettes are depicting the god Osiris wearing his standard attire. As it is clear in Figure 1. It grasps a *nekhakh* flail (usually held in the right hand) symbolized the north or Lower Egypt and a short-handled heka crook (in his right hand) represented the south or Upper Egypt and crowned with atef [27]. The four statuettes (1- 4) measure 7.2, 7.4, 9.4, and 9.75 cm respectively. The solid casting process was used in the manufacturing technique of the gilt-bronze statuettes. The effects of insatiability of the burial conditions lead to heterogeneous of the surface by formed various corrosion phases such as Cuprite/ Cupric salts as shown in figure 2.

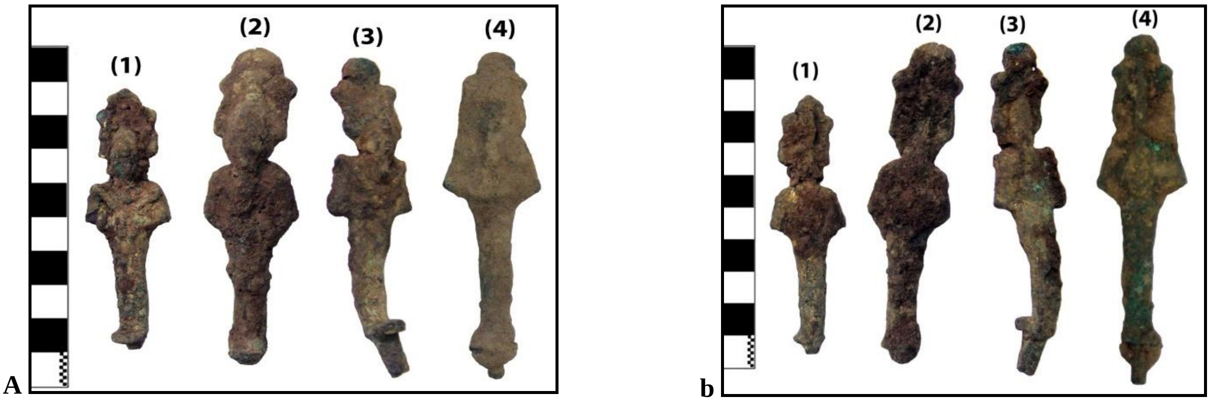

Figure 1: The four statuettes before conservation and treatment from front (a) and back (b), respectively

Figure 2: Close image of the four statuettes respectively showing the damage from soil deposition adhering with corrosion products and gold remain

Analysis techniques

A visual examination of each statuette was undertaken in order to assess the bronze patina morphology and to determine the corrosion products. Four Gilt-Bronze statuettes preserved at Kom Oshim storage were characterized using USB, Optical microscopes, and Confocal micro-Raman spectroscopy, and Portable X-Ray Fluorescence (p-XRF). Separated solid and powder samples from the four statuettes were collected for understanding of corrosion mechanism in the burial environment. The study of samples from different statuettes, which had certainly degraded through the burial, representing the different corrosion phases.

USB Microscope

Examinations in situ were performed by Dino-Lite USB digital microscope to detect gilding residues and study corrosion phases of the statuettes.

Optical Microscopy

The optical images have been recorded with a homemade TIRF microscope equipped with a Cmos camera and inverted microscope IX83 from Olympus Germany illuminated with high collimated white light from the high-intensity white led source as a laser-like source. In this regime, an oil-immersed UPLAPO100XOHR objective with NA=1.5 from Olympus. Samples were flipped over a coverslip #1, size 24x30 from Menzel Gläser Germany.

Confocal micro-Raman spectroscopy

Raman spectra and maps were recorded using a Confocal micro-Raman spectroscopy from Witec-Ulm Germany model Alpha300 RA/S, the used laser line was 532 nm laser. The used objective in Raman mapping was Zeiss EC Epiplan-Neofluar HD Dic 100x/0.9. Laser power density optimization is of great importance to collect the best Raman intensity without burning the sample or eliminating the corrosion layers, on the other hand it is very important to collect enough photons. In this regime, a beamed master laser power meter and beam profiler from the Coherent USA have been utilized by focusing the laser beam on the beam power meter sensor. In this work, the optimum laser power is 3.1 mW, the accumulation time was 150s for every spectrum. The selection of the mapping area depends on the largest flat squares which vary from 15 µm to 25 µm side length with a variable number of points per line to fix the images' resolution. The exposer time in mapping was 5s per point, while in single point measurement 30 spectra have been accumulated for every sample with the same exposer time. The resolving part in the spectrograph was 600g/mm grating with BLZ= 500 nm. The laser power is gradually and carefully increased to improve the signal to noise ratio, for this business single point is selected on the far edge of the sample, then exposed to the laser beam with different powers every time the exposed spot is investigated by scanning confocal microscope to detect if the exposed area damaged or not. A database covering the identifying Raman spectra was established.

Portable X-Ray Fluorescence

X-ray fluorescence results of statuette surface are given as a qualitative and quantitative of major elements. In Situ, *P*XRF analysis has been utilized to determine the elemental chemical composition of the statuettes. A handheld XRF model Tracer 5i from Bruker was used for this purpose. These techniques can provide valuable information on the technological process of gilding and mechanisms of deterioration.

3. Results and discussions

Microscopic USB examinations showed that gilded areas were adhered to copper basic salts and copper oxides and above them are the soil deposits (Figure 3). Thus, gold was lost when copper corrosion products were increased. A periodic phenomenon of solubilization, migration, and recrystallization occurs across the gold pores with the spread of copper salts on the surface in aggregates form, and the gilding layer sometimes detached, causing it to separate from the surface of the metal due to the progressive swelling corrosion products. A malachite may be formed as a fine stratum of Cu_2O. As a bi-product for the reaction between Cu/CuO_2 with $(CO^3)^{-2}/(HCO3)^{-1}$ group, the malachite ($Cu_2CO_3(OH)_2$) could be formed as a good water-soluble compound [31]. As a result of the malachite layer on the bronze surface, a patina grew on the bronze surface. Azurite ($2CuCO_3.Cu(OH)_2$) also could be regarded as such an isomer of malachite which is rarely reported in the literature as a resulting copper-alloy corrosive compound [29]. During burial or after excavation, chloride ions may lead to the formation of nantokite (CuCl), which could be regarded as a father of atacamite/paratacamite if an environment of humidity and oxygen gas have been achieved [30].

Optical Microscopy

Total internal reflection microscopy shows good snapshots for the examined areas. Unfortunately, in the case of statuette 1, there was no separated corrosion products for imaging, so for this statuette, we did not have any images or maps. Figure 4 (a) presents a cross section of the corroded gilded surface of statuette 2, gilding layer is located above green and red patina over the bronze surface. Figure 4 (b) shows domination for the green patina with some degradation spots with black and light blue in statuette 3. Figure 4 (c) presents a very small specimen of gold leaf embedded in corrosion products from statuette 4, was separated from the surface by the degradation of the adhesive material. It is noticed that there are some areas out of focus, as it is clear in Figure 4 (a) and (c); this comes from the uneven corroded surface of the statuettes.

Raman Micro-Spectroscopy

Raman mapping have been carried out recording the scattered radiation of the sample surface after illuminating the sample using a laser beam with a wavelength of approximately 532 nm. After carrying out the Raman analysis some signal processing was done like something and deconvolution to resolve the overlapped bands and hidden shoulders.

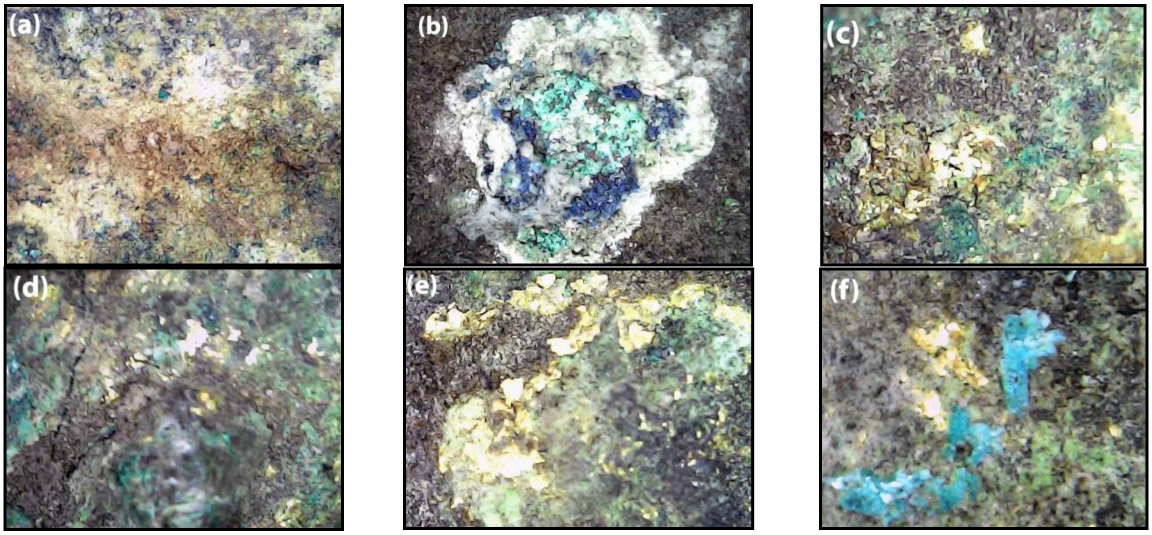

Figure 3. In situ microscopic images of the corrosion morphology show gilding remnants embedded inside blue and green corrosion products mixed with terrestrial deposits.

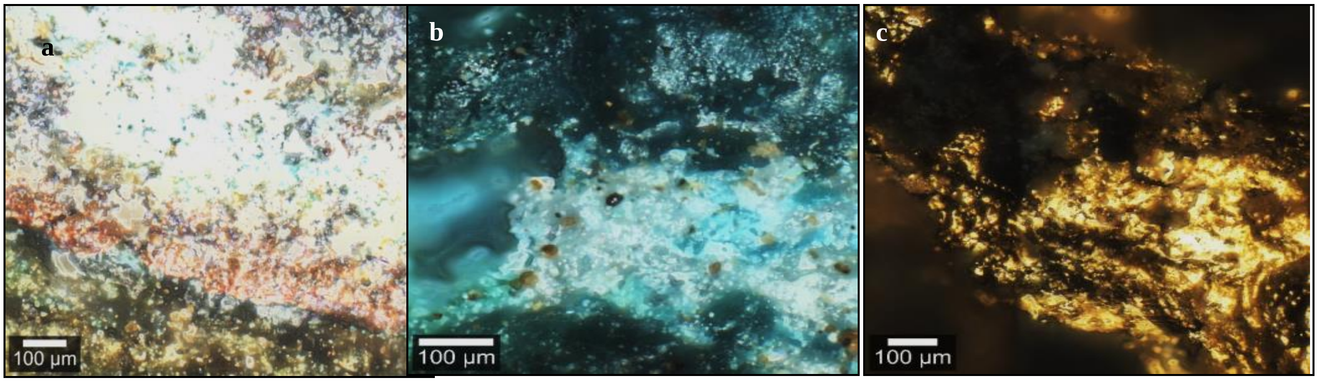

Figure 4: Total internal reflection imaging for sample **a)** statuette 2, **b)** statuette 3, and **c)** statuette 4. It is clear the blue and green patina in statuette 2 and 3 while that piece from statuette 4 shows small specimen of gold leaf

Statuette No.1

Figure 5 presents the Raman spectra of Statuette 1, which identify corrosion products of cooper, tin and lead according to the Raman bands assigned in Table 1. Cuprite (Cu_2O) was observed at a moderate band 153 cm^{-1}, besides a very weak band 629 cm^{-1}. The first two Raman bands refer to tenorite (CuO) in nanostructure at 286 and 333 cm^{-1}, besides a very weak band at 343 and 629 cm^{-1} [28], while the last two weak bands refer to bulk tenorite (CuO), these points need more investigation with additional techniques to confirm the presence of nanostructure in such ancient statues.

Copper-based compounds such as Azurite ($2CuCO_3.Cu(OH)_2$), botallackite ($Cu_2(OH)_3Cl$), brochantite ($CuSO_4.H_2O$), and verdigris ($Cu\ (CH_3COO)^{-2}.\ Cu(OH)_2$) were present in the Raman spectra shown in Figure 6. Azurite was observed at 110, 139, 246, 399(vs), 738(m), 646, 761, 767, 1095, 1422, 1429,1460, 1577 cm^{-1}. Botallackite ($Cu_2(OH)_3Cl$) was detected at 153, 246(s), 454, 399(vs) cm^{-1}. Brochantite ($CuSO_4.H_2O$) was seen at 778, 972 cm^{-1}. The copper acetate, Verdigris ($Cu\ (CH_3COO)^{-2}.Cu(OH)_2$) was present in the Raman spectra at 929, 935, 1060, 1413, 1551. The acetate ion in some of the corrosion products probably comes from one of two sources, from the wooden trays and cupboards used to store many objects after excavation, or from wood in the burial environment, or the wooden boxes that were sometimes used for the burial of groups of statuettes [25-32]. Casseterite (SnO_2) is also observed at 112, 210, 477, 638, and 778 cm^{-1}, the first two bands are related to bulk Tin Oxide, while the last three bands are related to nano tin Oxide [21]. The presence of Hematite is clear from the bands at 226, 285, 292, 543, 816, 1193, and 1321 cm^{-1} [33, 34]. Lead compounds has been noticed through the presence of the PbO_2 at 131, 139, 355, and 506 cm^{-1}, and anglesite ($PbSO_4$) at 972 cm^{-1}.

Galena (PbS) is also reported at 153, 454, and 834 cm^{-1}. Lead corrosion products could be attributed to the presence high lead content in the alloy. Complete assignment of the Raman spectra in Figure 5 is tabulated in Table 1.

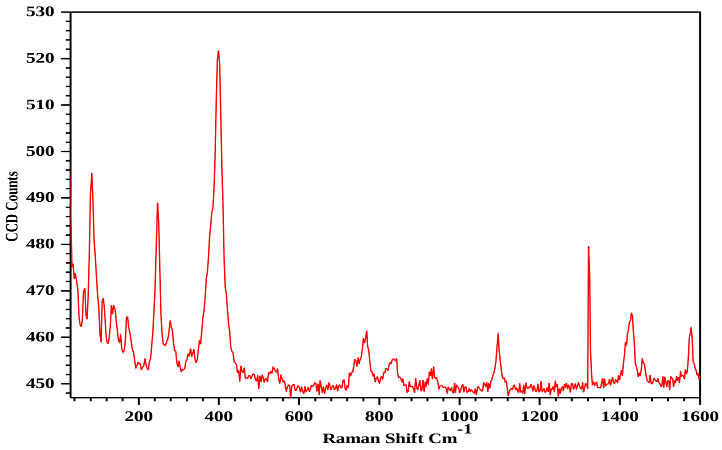

Figure 5: The Raman spectra of statuette No. 1 as scattered by irradiating the sample with 532nm laser with power 1mW and Ziss HD Dic 100x / 0.9 objective.

Table 1: Raman bands of statuette No. 1

Name	Composition	Detected Raman bands [cm^{-1}]	Ref.
Cuprite	Cu_2O	153, 629	39
Tenorite	CuO	286, 333,343,629	31
Botallackite	$Cu_2(OH)_3Cl$	153, 246, 454, 399	39
Brochantite	$CuSO_4.H_2O$	778, 972	54
Azurite	$2CuCO_3.Cu(OH)_2$	110, 139, 246, 399, 738, 646,761,767, 1095, 1422, 1429,1460, 1577	45
Verdigris	$Cu(CH_3COO)^-_2. Cu(OH)_2$	929,935, 1060, 1413, 1551	31
Red Lead	Pb_3O_4	65, 82 , 153	47
Plattnerite	α-PbO_2	131, 139, 355, 506	58
Anglesite	$PbSO_4$	972	65
Lead Sulfide	PbS	153, 454, 834	48
Casseterite	SnO_2	112, 210, 477, 638, 778	66
Hematite	Fe_2O_3	226, 285, 292, 543, 816, 1193, 1321	57

Statuette No.2

Figure 6 (a) shows the Raman spectra of Statuette 2, like Statuette. Tenorite (CuO), cassitrite (SnO_2), and hematite (Fe_2O_3) were present in the spectra in the same band positions. Also, lead compounds Pb_3O_4, PbO_2, $PbSO_4$, and PbS were reported as mentioned before. The new Raman bands that appear in this sample will be assigned in Table 2. It is also noticed the presence of cerussite ($PbCO_3$) at 109 cm^{-1} which could be attributed to corrosion of lead in the chemical structure of the alloy. During casting it is possible to get some segregation of the lead to the outer surface of the mold, with the result that there may be a prevalence of lead-containing corrosion products, such as the commonly encountered cerussite and hydrocerrusite, in the patina [25].

Hematite and magnetite show its characteristic band at 660 cm^{-1}. The presence of the amid band at 1284 cm^{-1} and the Carboxyl band at 1745 cm-1 could be regarded as a piece of evidence about the presence of micro-organisms and their metabolisms, also the C=O could be regarded as an indicator about the humic acids.

Bands at 930 and 1030 cm^{-1} were attributed to the presence of AlO_4, and that at 775, 1065, and 1199 cm^{-1} attributed to SiO_2. In case of the presence of both Silica and Aluminum Oxide, it will be normal to identify Aluminum Silicate at 557 and 1160 cm^{-1}. Single-band attributed to Actinolite ($Ca_2Fe_5Si_8O_{22}(OH)_2$) located 232 cm^{-1} from the laser line. Copper minerals appeared over the scanned area, two green minerals the malachite green which detected only a single Raman band at 1614 cm^{-1} while the rest were very weak the second is the Verdigris which detected through the appearance of the Raman bands at 181, 324, 477, 680, 1536, and 1648cm^{-1}. From the distribution and intensities of malachite, and verdigris it's equally distributed over the sample. It is detected also the presence of Copper Chloride mineral named Paratacamite (Copper Trihydroxychlorides) at 367, 474, 513, and 896 cm^{-1}. The presence of C=O resonates at 1573 cm^{-1}.

Figure 6 (b) to (q) shows the distribution of the assigned bands over the flattest scanned area, the color mapping shows the intensity distribution in the z-direction which is variable according to the real distribution of the compounds.

From Figures 6 (b) and (c), one could estimate that the content of the Lead compounds tends to reach 50% of the corrosion products, the underestimation because of the possibility of lead globules in the alloy. Hematite and tin Oxide are equally distributed over the scanned area as presented in Figures 6 (e) and (f). In Figure 6 (d), one could notice the equal distribution of white lead in the TIRF image presented in Figure 4 (a), in this figure the distribution of white spots is also distributed over the whole area.

The distribution of the Aluminium Silicate (Si-O-Si) Al is also the same as the distribution of Si-O-Si with the same intensity which is normal. Regarding the nano CuO and Bulk CuO, one could easily notice that the higher intensities are distributed in the bulk CuO in the lower right corner while in the same area in the nano tenorite (CuO) is the intensities is lower according to the color mapping, it is also important to put in consideration that the highest counts in nano CuO are 13 CCD counts and in the bulk one the highest counts are only 7, this could be attributed to the presence of the humic acids which could help in gathering the CuO particles in bulk structures as degradation process. Through Figure 6 (p) and (q), one could easily see the will distribution of the Amid and Carboxyl groups which are a strong indicator about the presence of micro-organisms and their metabolism and the humic acids in burial environment.

Table 2: Raman bands Statuette No.2

Name	Composition	Detected Raman bands [cm^{-1}]	Ref.
Paratacamite	$Cu_2(OH)_3Cl$	367, 474, 513, 896	43,44
Hydrocerrusite	$2PbCO_3{\cdot}Pb(OH)_2$	109, 412	58, 64
Hematite	Fe_2O_3	660	57, 60
Aluminate	AlO_4	930, 1030	40
Quartz	O-Si-O	775, 1065,1199	51
Aluminum Silicate	Si-O-Si(Al)	557, 1160	53
Actinolite	$Ca_2Fe_5Si_8O_{22}(OH)_2$	232	53
Carboxyl	C=O	1573, 1745	45
Amide	N-C=O	1284	45

Statuette No.3

Figure 7 and Table 3 show the Raman study of Statuette 3 like in the previous sample, an averaging over all the areas has been carried out. Following the Raman bands, one could easily notice the presence of red lead, PbO_2, PbS, and $PbSO_4$ the distribution of those compounds is presented in Figures 4 (b) and (c). Also, the presence of SnO_2 and CuO as in Statuette (1), there are nano and bulk bands, the hematite and magnetite are also found with good distribution over the sample as presented in Figures 7 (f), (g), (h), and (i). By noticing the TIRF image of statuette (3) in Figure 7 (b), one could see easily the black spots which are attributed to the formation of Pbs, PbO_2, and $PbSO_4$. Also, white spots could be attributed to the presence of $2PbCO_3{\cdot}Pb(OH)_2$, the distribution in the Raman mapping in Figure 7 (d) looks the same as the white spots in Figure 4 (b). As it is presented in Figure 7 (j), (k), and (l) the corrosion products distribution over the sample has some differences.

Statuette No.4

Figure 8 (a) is presenting the Raman spectra of statuette 4, which shows some differences from the previously measured samples. Lead corrosion products are also present, but in this sample, lead Oxalate is detected. lead Oxalate resulted in corrosion products was formed through the activity micro-organisms and their metabolism. The distribution of lead compounds in the corrosion layer was presented in Figure 8 (b), (c), (e), and (f), as it is clear in Figure 4 (c). The stability and very low solubility of these compounds support the hypothesis of a protective role which would then explain the good state of preservation of the object [32]. Regarding the metal compounds, the nano and bulk tenorite (CuO) and SnO_2 were present also in Figures 8 (h), (i), and (p) still like the previous we have double the intensities for the nano CuO map in comparison with the bulk CuO. Malachite is formed in this area as brittle spots and distributed equally with fewer CCD counts around 5 counts with very few spots having high concentration as it is shown in Figure 8 (g). Regarding the SiO2 and Al Silicate Figures 8 (k), and (m) show approximately equally distributed concentrations over the whole area. Cassiterite SnO_2 was observed at 474 cm^{-1}. The distribution of Paratacamite is also affected by the strong corrosion with a diagonal high distribution like the other compounds in this map, Table 4 presents the Raman bands

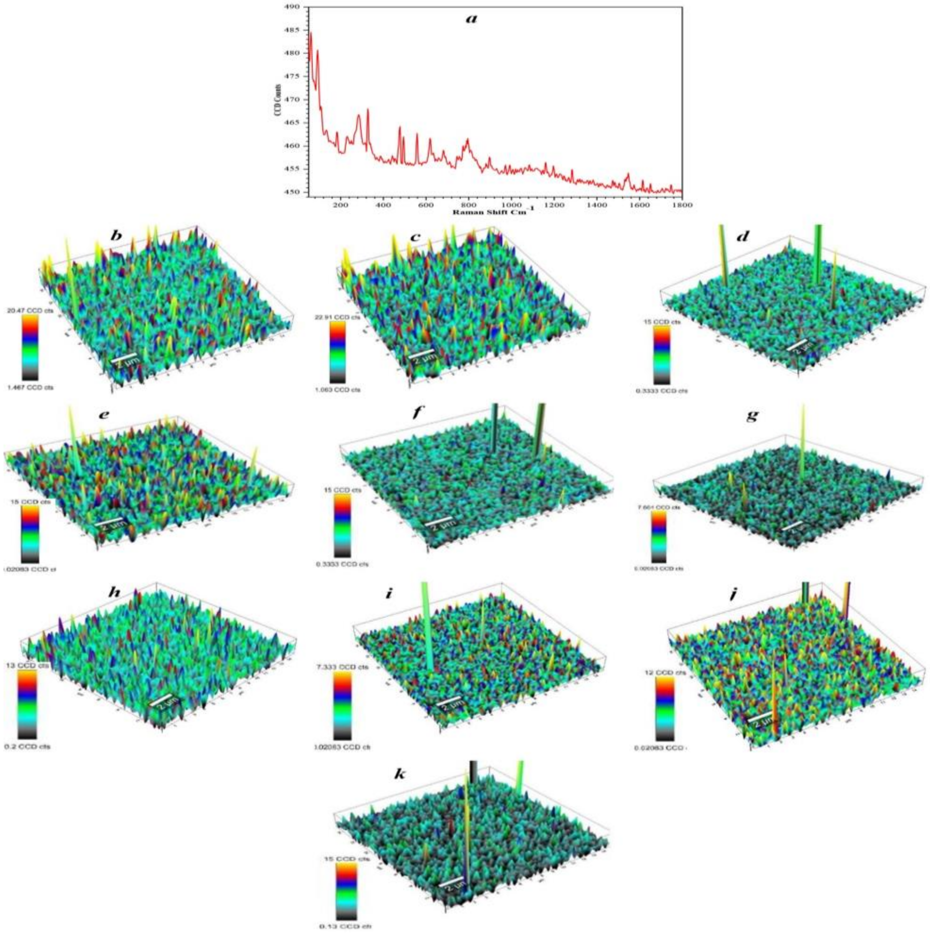

Figure 6: Raman spectra and Mapping of the statuette No. 2 a) Raman spectra of the sample averaging over the total mapped area, the distribution of the b) Pb_3O_4, c) PbO_2, d) SnO_2, e) AlO_4, f) Al silicate, g) SiO_2, h) nano CuO, i) Bulk CuO, j) Amide, k) Carboxyl bands. The scanned area was 15×15 µm divided into 75×75 point with laser power 1mW and accumulation time 5s for every pin

Table 3: Raman bands of Statuette No.3

Name	Composition	Detected Raman bands [cm^{-1}]	Ref.
Tenorite	CuO	286, 333,343,629	66
Paratacamite	$Cu_2(OH)_3Cl$	474, 501, 513, 732, 890	44
Plattnerite	α-PbO_2	131, 139, 355, 506	58
Casseterite	SnO_2	112, 210, 477, 638, 778	66; 67
Lead Sulfate	$PbSO_4$	972	65
Lead Sulfide	PbS	153, 454, 834	48
Hematite	Fe_2O_3	491, 660	34
Hydrocerussite	$2PbCO_3{\cdot}Pb(OH)_2$	109, 412	58,64

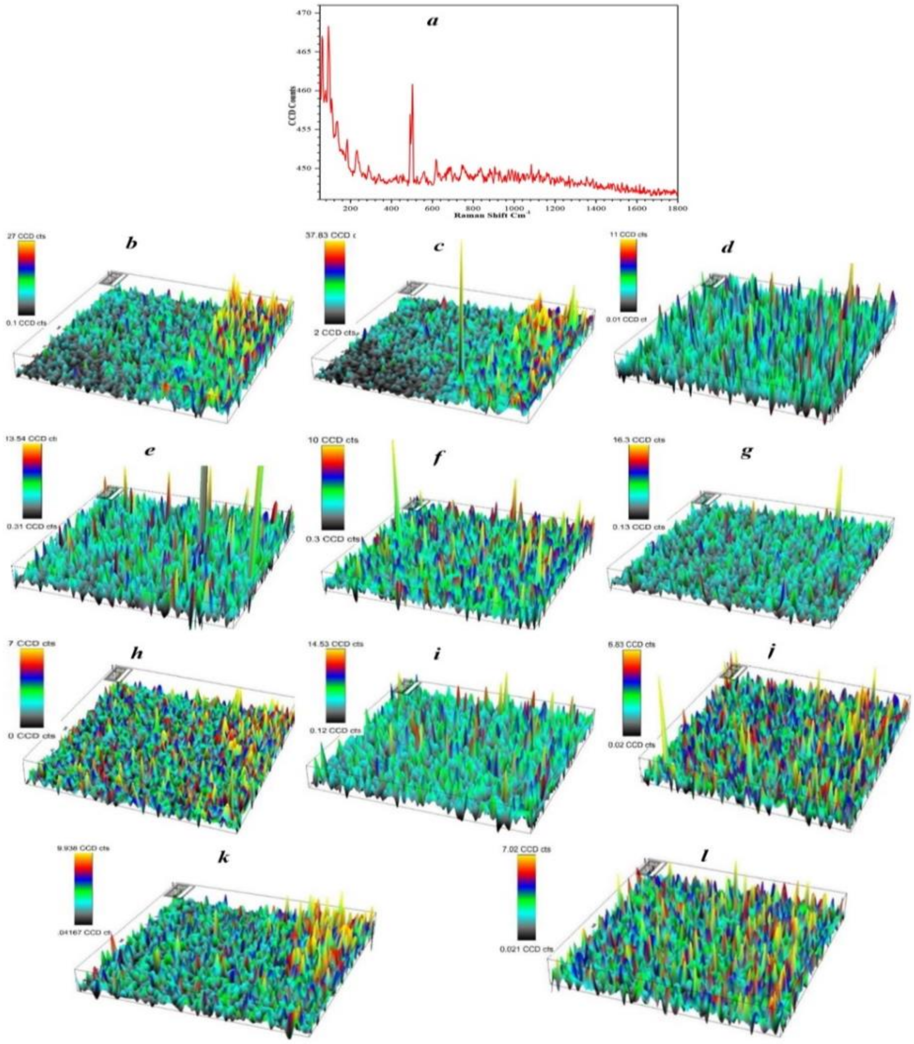

Figure 7: Raman spectra and Mapping of the Statuette No. 3 a) Raman spectra of the sample averaging over the total mapped area, the distribution of the b) Pb3O4 , c) PbO2, d) PbCO3, e) PbCrO4, f) Hematite, g) SnO2, h) Bulk CuO, i) nano CuO, j) Malachite, k) Verdigris, l) Paratacamite, bands. The scanned area was 20×20 µm divided into 75×75 point with laser power 1 mW and accumulation time 5 s for every pin.

.

Table 4: Raman bands of statuette No. 4

Name	Composition	Detected Raman bands [cm^{-1}]	Ref.
Tenorite	CuO	286, 333, 386,617, 629	66
Red Lead	Pb_3O_4	65, 82, 153	47
Plattnerite	α-PbO_2	92, 156,	58
Whit Lead	Pb_3O_4	63,109	58
Galena	PbS	444	48
Lead Oxalate	PbC_2O_4	574,890,1401,1480	58,64
Lead Sulfate	$PbSO_4$	972	65
Paratacamite	$Cu_3(OH)_6C_{l2}$	367, 440, 474,501, 513, 732	44
Aluminum Silicate	Si-O-Si(Al)	557,1158	53
Quartz	Si-O-Si	550	40
Casseterite	SnO_2	639	66
Aluminate	AlO_4	922, 928	47
Aluminate	AlO_4	922, 928	53

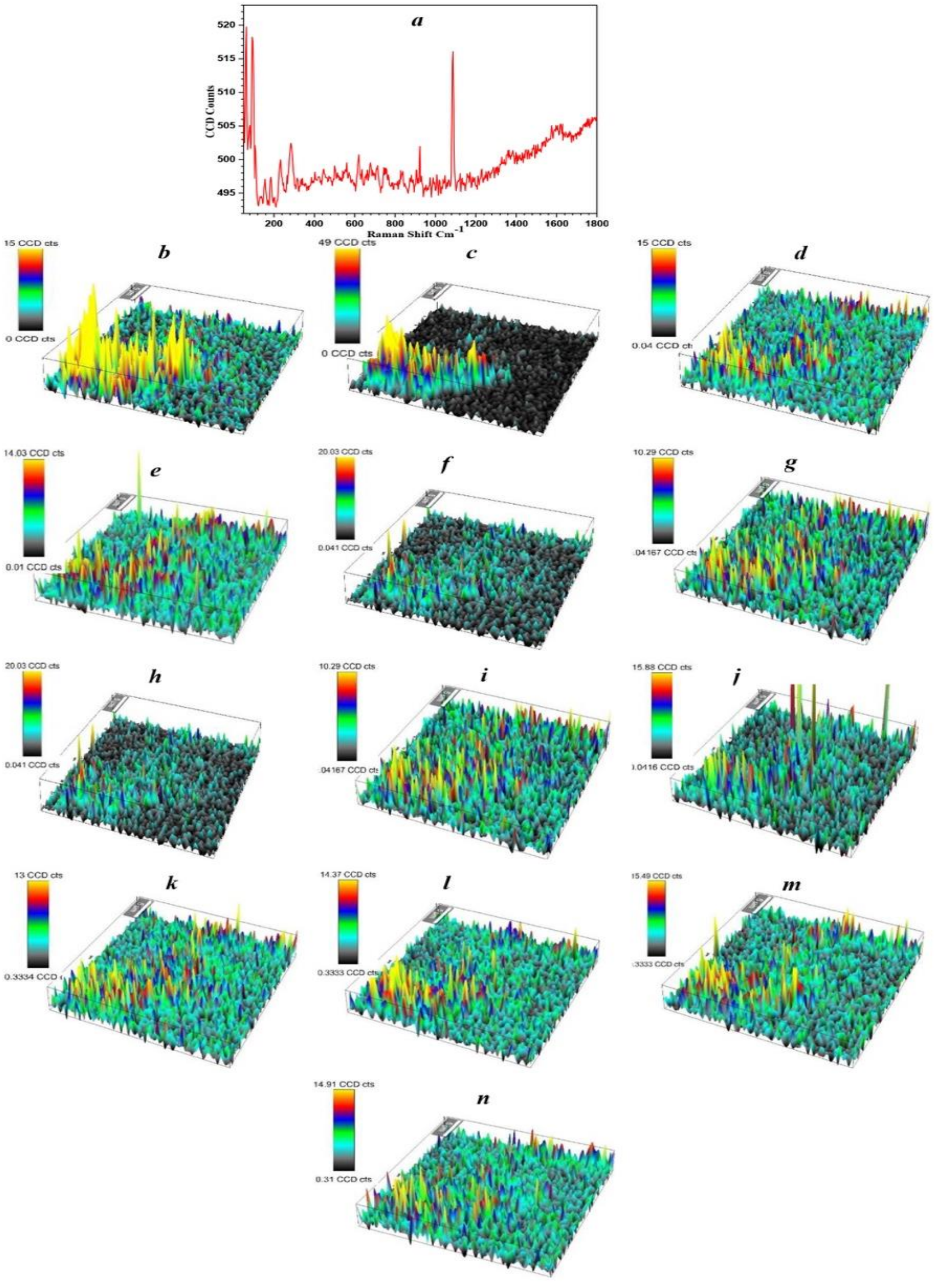

Figure 8: Raman spectra and Mapping of the statuette No.4 a) Raman spectra of the sample averaging over the total mapped area, the distribution of the b) Pb_3O_4, c) PbO_2, d) $PbCrO_4$, e) PbO, f) PbC_2O_4, g) $CuCO_3$, h) nano CuO, i) Bulk CuO, j) AlO_4, k) SiO_2, l) Paratacamite, m) (Si-O-Si)Al, n) SnO2 bands. The scanned area was 25×25 μm divided into 75×75 point with laser power 1mW and accumulation time 5s for every pin.

X-Ray fluorescence

The XRF data shows evidence of such interaction between the soil ingredients and the surrounding elements like Cl, Ca, Al, K, and Fe, with the bronze components that form a variety of corrosion products. Table 5 presents the elements and their percentage in the analyzed spots. In the tabulated data, Cu is the main alloying element, lead (Pb) percentages varied from 8.23% to 12.56% weight per weight). Sn is also clear in the table with percentages from 2.75% to 3.81% weight per weight. It is well known that leaded bronze alloy was extensively used for making small statues [24, 36, 37]. Many tin bronzes are leaded. In low-tin bronzes, typically used for castings, the lead does not alloy with the copper or the tin and occurs as small globules throughout the metallic structure [25]. During casting it is possible to get some segregation of the lead to the outer surface of the mold, with the result that there may be an occurrence of lead-containing corrosion products in the patina. The effects of lead, when present as a major alloying constituent in leaded bronzes are a gradual linear reduction of tensile strength, elongation, hardness, and a gradual increase in density [38]. The presence of gold content ranged from 3.56 % to 5.43% wt. that indicating the presence of gilding residues.

Treatment procedures

Treatment methods were totally accomplished using fine and simplest hand tools like scalpels and brushes under lens magnification with a lighting source to remove encrustations with great caution. Finally, the protection process of Osiris statuettes was accomplished using 3% Benzotriazole (BTA) and two layers of Permalac (ready to use). The statuettes were packed individually in a rigid polyethylene box which is well padded with acid-free tissue. Before padding the box, a layer of silica gel was inserted in the bottom, which provides an appropriate temperature and relative humidity, until the statuette will be transported to a controlled environment. Figure 9 shows the statuettes after the conservation processes.

Table 5: XRF results of elemental composition of the gilded statuette

	Alloy (Wt. %)			**Gilding (Wt. %)**	**Soil components (Wt. %)**						**Bronze disease (Wt. %)**
Element	**Cu**	**Sn**	**Pb**	**Au**	**Si**	**Mg**	**Ca**	**Al**	**Fe**	**K**	**Cl**
Statuette No.1	74.66	3.81	12.56	3.56	2.42	0.82	0.6	0.04	0.04	0.03	2.42
Statuette No.2	75.35	3.16	11.26	4.28	2.64	0.22	0.86	0.03	0.06	0.02	2.12
Statuette No.3	76.29	3.55	8.23	5.43	2.96	0.06	0.43	0.30	0.73	0.07	1.95
Statuette No.4	76.87	2.75	9.33	3.28	2.71	0.07	0.84	0.83	0.96	0.7	1.66

Image 9 (a,b): The gilded bronze statuettes after finishing the treatment processes

4. Conclusion

These experiments were done using Raman spectra on separated specimens targeted at the optimization of a dependable, non-destructive, and more accurate for characterization of micro-chemical structure of gilt-bronze statuettes. Both spectroscopic and microscopic analyses have been conducted on those statuettes, micro-chemical structure micrograph of the surface were assigned. Various phases of corrosion on gilt-bronze patina were detected in different Raman signatures such as cuprite, atacamite, paratacamite, and botalchite. Besides lead and tin corrosion products were detected such as: litharge, massicot, cerussite, cassiterite and hydrocerrusite. Copper-tin nanoparticles have been found in the samples, these nanostructures either formed from the corrosion process or it was original caused by the manufacturing process. According to XRF results, selected gilded statuettes were made of lead bronze represented the god Osiris. 3-5% gold contents indicate the presence of gilding residues. In the four statuettes, the gilding layer was damaged as a result of the accumulation of the corrosion yields, principally copper chloride hydroxide (atacamite) that are interfering with the gilding layer. Coating system composed of 3% benzotriazole (BTA) and two layers of permalac (ready to use) were applied for the long-term preservation.

5- References

1. Chiriu, D., Pisu, FA., Ricci, PC., Carbonaro, CM., Mater.2020,13,2456. https://doi.org/10.3390/ma13112456.
2. Sevgi, B., Kameray, Ö., Elif, S., Cuauhtémoc, A., Yılmaz, SE., Spectrochim Acta A 2020, 237,118311. https://doi.org/10.1016/j.saa.2020.118311.
3. Atta, D., Fakhry, A., Ibrahim, M., der Pharma Chem. 2015; 7:357-361.
4. Atta D., Ismail M.M., Battisha I.K., Opt. Laser Technol. 2022, 149, 107761. DOI:10.1016/j.optlastec.2021.107761
5. Refaat A., Atta D., Osman O., Mahmoud A.A., El-Kohadary S., Malek W., Ferretti M., Elhaes H., Ibrahim M., Biointerface Res. Appl. Chem. 2019, 9, 4685 - 4698. DOI:10.33263/BRIAC96.685698
6. Farrage N. M., Oraby A. H., Abdelrazek E. M., Atta D., Biointerface Res. Appl. Chem., 2019, 9, 3934– 3941. DOI:10.33263/BRIAC93.934941
7. Osman O., Mahmoud A., Atta D., Okasha A., Ibrahim M., Der Pharma Chem, 2015, 7, 377-380.
8. Ibrahim M., Elhaes H., Atta D., J. Comput. Theor. Nanosci., 2017, 14, 4114-4117. https://doi.org/10.1166/jctn.2017.6794.
9. Atta D., Gomaa F., Elhaes H., Ibrahim M., J. Comput. Theor. Nanosci., 2017, 14, 2405-2408, https://doi.org/10.1166/jctn.2017.6840.
10. Farrage N. M., Oraby A. H., Abdelrazek E. M., Atta D.,Egypt J. Chem., 2019, 62, 99-109. https://doi.org/10.21608/EJCHEM.2019.12746.1791
11. Galal A., Atta D., Abouelsayed A., Ibrahim M., Hanna A., Spectrochim. Acta. A, 2019, 214, 476-486. https://doi.org/10.1016/j.saa.2019.02.070.
12. Atta D., Okasha A., Spectrochim. Acta A 2015, 135,1173–1179. https://doi.org/10.1016/j.saa.2014.07.085.
13. Atta D., Okasha A., Ibrahim M., Der Pharm Chem 2016, 18, 76-82.
14. Charles M., J. Rheol., 2018, 62, 371-403. https://doi.org/10.1122/1.5013246.
15. Petrosyan R., Rheol. Acta, 2017, 56, 21-26. https://doi.org/10.1007/s00397-016-0977-9
16. Kartal F., Çimen D., Bereli N., Denizli A., Mater. Sci. Eng. C, 2018, 97, 730-737, https://doi.org/10.1016/j.msec.2018.12.086.
17. Knyazev M., Karimullin K., Naumov A., Phys. Status. Solidi. RRL., 2017, 11, 1600414. https://doi.org/10.1002/pssr.201600414.
18. Elbanna A., Atta D., Sherief D., In vitro bioactivity of newly introduced dual-cured resin-modified calcium silicate cement. Dental Research Journal2022;19,1.https://doi.org/HYPERLINK"https://dx.doi.org/10.4103%2F1735-3327.336686"10.4103/1735-3327.336686.
19. Andersen, E., Muggli, Z., Microscopical techniques in the use of the molecular optics laser examiner Raman microprobe. Anal Chem 1981;53:1772-1777, https://doi.org/10.1021/ac00235a013.
20. Charalambos, Z., Andreas, K., Paradellis, T., Development of X-ray fluorescence methods by use of a Mo X-ray tube and their application in the case of biological samples. NPS Advanc Nucl Phys 2019;11:2075. https://doi.org/10.12681/hnps. 2225.
21. Li, L., Zhaoshui, Y., Jinli, X., Yanshan, P., Wei, B., Bin, L., Pengpeng, Z., Jinfeng, B., Qin, Z., The technique of high-pressure powder pressing with polyester film covering for XRF of geochemical samples. X-Ray Spectrom 2020; 49:1– 11. https://doi.org/10.1002/xrs.3147.
22. Emma, F., David, B., Thomas, P., Simion, B., Nelson, K., Building ED-XRF datasets for sourcing rhyolite and quartzite artifacts: A case study on the Homa Peninsula, Kenya, J Archaeol Sci Reports 2020;33:102510. https://doi.org/10.1016/j. jasrep.2020.102510.
23. Tronner, K., Nord, G., Borg, C., Corrosion of archaeological bronze artefacts in acidic soil. Water Air Soil Pollut 1995;85:2725-2730. https://doi.org/10.1007/ BF01186246.
24. Alessandrini, G., Dassù, G., Pedeferri, P., Re, G., On the conservation of the baptistery doors in florence. Stud Conserv. 1979;24:108-124. https://doi.org/10.1179/ sic.1979.013.
25. Scott, A., Copper and bronze in art: corrosion, colorants and conservation, Getty Conservation Institute, Los Angeles. 2002.
26. Abdelbar, M., Ahmed, S., Conservation Treatment and Analytical Study of Egyptian Gilded Bronze Statue of Seated Osiris, Int J Conserv Sci 2021;12:1407-1420.
27. Gravett, F., A Critical Analysis of Selected Egyptian Bronze Artefacts in the National Cultural History Museum (Nchm), Master Thesis, University of South Africa 2011.
28. Guisti, A., Matteini, M., The Gilded Bronze Paradise Doors by Ghiberti in the Florence Baptistery. Scientific Investigation and

Problems of Restoration, Paper presented at the International Conference on Metal Restoration organized by the Bavarian State Conservation Office and the German National Committee of ICOMOS, Munich, 1997,23-25 october. https://doi.org/10.11588/ih.1998.0.23180.

29. Fiorentino, P., Marabelli, M., Matteini, M., Moles, A., The condition of the ‘Door of Paradise’ by L. Ghiberti. Tests and proposals for cleaning. Stud Conserv 1982;27:145-153. https://doi.org/10.1179/sic.1982.27.4.145.
30. Qudbashi, O., The condition of the ‘Door of Paradise’ by L. Ghiberti. Tests and proposals for cleaning. Surf Interface Anal 2015;47:1133–1147. https://doi.org/10.1179/sic.1982.27.4.145.
31. Rashad, M., Rüsing, M., Berth, G., Lischka, K., CuO and Co_3O_4 Nanoparticles: Synthesis, Characterizations, and Raman Spectroscopy. J Nanomater 2013;714853. https://doi.org/10.1155 /2013/714853.
32. Paterakis, A., The Formation of Acetate Corrosion on Bronze Antiquities: Characterisation and Conservation, PhD thesis, University College London, London 2010.
33. Houda, M., Hanen, L., Radhouane, B., Sonia, D., Beatrice, N., Cécile, A., Abdellatif, G., Salah, A., Structural, optical, magnetic and electrical properties of hematite (α-Fe2O3) nanoparticles synthesized by two methods: polyol and precipitation. Appl Phys A:Solids Surf 2017;123:787. https://doi.org/10.1007/s00339-017-1408-1.
34. Nicolae, B., Andrei, I., Vasile, D., Andrei, B., The Raman study of amphiboles. Analele Stiintifice ale Universitatii “Al. I. Cuza” din Iasi Seria Geologie. 2013;59,5–22.
35. Remazeilles, C., Conforto, E., A Buried Roman Bronze Inkwell: Chemical Interactions With Agricultural Fertilizers, Stud in Conserv. 2008;53:110-117.
36. Ghoniem, M., The characterization of a corroded Egyptian bronze statue and a study of the degradation phenomena, Int J Conserv Sci 2011;2:95–108.
37. Gouda, K., Youssef, I., AbdelGhany, A., Characterization of Egyptian bronze archaeological artifacts, Surf. Interface Anal 2012;44:1338–1345. 10.1002/sia.5029
38. Robbiola, L., Hurtel, P., Standard nature of the passive layers of buried archaeological bronze: The example of two Roman half-length portraits, In METAL 95: International Conference on Metals Conservation, MacLEod I, Pennec S, Robbiola L. Eds., James &James Science Pub., London 1997:109-117.
39. Zhang, S., Spectroscopy and its Application in Nanostructures, Analytical and Bioanalytical Chemistry 2012; 404, 2524.
40. Avadhesh, Y., Prabhakar, S., A review of the structures of oxide glasses by Raman spectroscopy. RSC Adv 2015;5:67583–67609. https://doi.org/10.1039/ C5RA13043C.
41. Calparsoro, E., Maite, M., Hector, M., Gorka, A., Iñañez, G., Non-destructive screening methodology based on ED-XRF for the classification of medieval and post-medieval archaeological ceramics. Ceram Int 2019;45:10672-10683. https://doi.org/10.1016/j.ceramint.2019.02.138.
42. Carvalho, R., Munita, S., Neves, G., Zimpel, A., A preliminary assessment of the provenance of ancient pottery through instrumental neutron activation analysis at the Monte Castelo site, Rondônia, Brazil. J Radioanal Nucl Chem 2020;324:1053–1058. https://doi.org/10.1007/ s10967-020-07143-3.
43. Francesca, B., Paolo, P., Paolo, D., Marisa, T., The formation of metal oxalates in the painted layers of a medieval polychrome on stone, as revealed by micro-raman spectroscopy. Stud Conserv 2008;53:158–169. https://doi.org/10.1179/sic.2008. 53.3.158
44. Frost, R., Martens, W., Kloprogge, T., Williams, A., Raman spectroscopy of the basic copper chloride minerals atacamite and paratacamite: implications for the study of copper, brass and bronze objects of archaeological significance. J Raman Spectrosc 2002;33:801-806. https://doi.org/10.1002/jrs.921.
45. Ian, M., Robin, J., Peter, J. Raman spectroscopic library of natural and synthetic pigments (pre- ≈ 1850 AD). Spectrochim Acta A 1997;53:2159-2179. https://doi.org/10.1016/S1386-1425(97)00140-6.
46. Louisa, M., Arthur, R., Frederik, V., Koen, J., Synchrotron-Based High-Energy X-ray MA-XRF and MA-XRD for Art and Archaeology. Synchrotron Radiat News 2019;32:29-33. https://doi.org/10.1080/08940886.2019.1680212
47. Lucia, B., Robin, J., Steven, F., Raman spectroscopy as a means for the identification of plattnerite (PbO_2), of lead pigments and of their degradation products. Analyst; 2001;126:222–227. https://doi.org/10.1039/b008302j.
48. Mohsen, C., Ramin, Y., Farid, J., Abdolhossein, S., Comparative study of Raman properties of various lead sulfide morphologies. M J T D 2013;2:163-166.

http://journals.iaumajlesi.ac.ir/td/index/index.php/td/article/view/90.

49. Okasha, A., Atta, D., Badawy, M., Frontasyeva, V., Elhaes, H., Ibrahim, M., Modeling the coordination between Na, Mg, Ca, Fe, Ni, and Zn with organic acids. J Comput Theor Nanosci 2017;14:13571361. https://doi.org/10.1166/jctn.2017.6457.

50. Petrosyan, R., Improved approximations for some polymer extension models. Rheol Acta 2017;56:21-26. https://doi.org/10.1007/s00397-016-0977-9.

51. Quiles, F., Burneau, A., Infrared and Raman spectra of alkaline-earth and copper(II) acetates in aqueous solutions. Vib Spectrosc 1998;16:105–117, https://doi.org/10.1016/S0924-2031(98)00004-6.

52. Smith, D., Firth, S., Clark, H., Cardona, M. First- and second-order Raman spectra of galena (PbS). J App Phys 2002;92:4375–4380, https://doi.org/10.1063/1. 1505670.

53. Stefanovsky, V., Fox, K., Marra, J., Infrared and Raman Spectroscopic Study of Glasses in the Al_2O_3-B_2O_3-Fe_2O_3-Na_2O-SiO_2 System. MRS Online Proc Libr 2013;1518:53–58. https://doi.org/10.1557/opl.2013.143.

54. Hayez, V., Guillaume, J., Hubin, A., Terryn, H., Micro-Raman spectroscopy for the study of corrosion products on copper alloys: setting up of a reference database and studying works of art, J. Raman Spectrosc. 2004;35: 732–738.

55. Fan, X., Wang, Q., Wang, Y., Non-destructive in situ Raman spectroscopic investigation of corrosion products on the bronze dagger-axes from Yujiaba site in Chongqing, China, Archaeological and Anthropological Sciences 2020;12: 90.

56. Bongiorno, V., Campodonico, S., Caffara, R., Piccardo, P., Carnasciali, M., Micro-Raman spectroscopy for the characterization of artistic patinas produced on copper-based alloys, J. Raman Spectrosc. 2012;43:1617–1622.

57. Neff, D., Reguer, S., Bellot-Gurlet, L., Dillmann, P., Bertholon, R., Structural characterization of corrosion products on archaeological iron: an integrated analytical approach to establish corrosion forms, 2004, 35, 8-9: 739-745

58. Costantini, I., Lottici, P., Bersani, D., Pontiroli, D., Casoli, A., Castro, K., Madariaga, J., Darkening of lead- and iron-based pigments on late Gothic Italian wall paintings: Energy dispersive X-ray fluorescence, μ-Raman, and powder X-ray diffraction analyses for diagnosis: Presence of β-PbO2 (plattnerite) and α-PbO2 (scrutinyite), 2020; 51: 680-692

59. Colomban, P., Tourni, L., Maucuer, M., Meynard, P., On-site Raman and XRF analysis of Japanese/Chinese bronze/brass patina – the search for specific Raman signatures, J. Raman Spectrosc. 2012;43:799–808.

60. Ahmed, S., Corrosion mechanism of iron objects in marine environment an analytical investigation study by raman spectrometry, European J. of Science and Theology, 2017; 13: 185-206

61. Franquelo, M., Duran, A., Herrera, K., Jimenez de Haro, C., Perez-Rodriguez, L., Comparison between micro-Raman and micro-FTIR spectroscopy techniques for the characterization of pigments from Southern Spain Cultural Heritage, Journal of Molecular Structure 2009;924–926:404-412.

62. Monnier, J., Bellot-Gurlet, L., Baron, D., Neff, D., Guillot, I., Dillmann, H., A methodology for Raman structural quantification imaging and its application to iron indoor atmospheric corrosion products, J. Raman Spectrosc. 2011; 42:773-781.

63. Veneranda, M., Costantini, I., De Vallejuelo, S., Garcia, L., Garcia, I., Castro, K., Azkarate, A., Madariaga, M., Study of corrosion in archaeological gilded irons by Raman imaging and a coupled scanning electron microscope–Raman system, Philosophical Transaction R. Soc. A 374: 20160046. http://dx.doi.org/10.1098/rsta.2016.004

64. Ilaria, C., P. L. Pier, C. Kepa and M. M. Juan. 2020.“ Use of Temperature Controlled Stage Confocal Raman Microscopy to Study Phase Transition of Lead Dioxide (Plattnerite), *Minerals*, 10, 2020, 468, https://doi.org/10.3390/min10050468.

65. Alexander, B., E. Ellen, R. Eckart, F. Roman and B. Daniel.2007.“ On the use of Raman microscopy for sulfation analysis in lead-acid battery research“ *Journal of Energy Storage*, 12:305–310. https://doi.org/10.1016/j.est.2019.101047.

66. Li, X., Y. Liu, S. Li, J. Huang, Y. Wu and D. Yu.2016. “ The Sensing Properties of Single Y-Doped SnO_2 Nanobelt Device to Acetone“ *Nanoscale Research Letters*, 11:470. doi:10.1186/s11671-016-1685-1.

Guo, X.W., X.P. Fang, Y. Sun, L.Y. Shen, Z.X. Wang and L.Q. Chen.2013.“ Lithium storage in carbon-coated SnO_2 by conversion reaction“ *Journal of Power Sources*, 226:75-81. https://doi.org/10.1016/j.jpowsour.2012. 10.068